Deglacial upwelling, productivity and CO_2 outgassing in the North Pacific Ocean

William R Gray[1,2], James W B Rae[2], Robert C J Wills[3], Amelia E Shevenell[4,5], Ben Taylor[2], Andrea Burke[2], Gavin L Foster[6], Caroline H Lear[7]

[1]Department of Geography, University College London, UK

[2]School of Earth and Environmental Sciences, University of St Andrews, UK

[3]Department of Atmospheric Sciences, University of Washington, Seattle, WA, USA

[4]Department of Earth Sciences, University College London, UK

[5]College of Marine Science, University of South Florida, Tampa, FL, USA

[6]Ocean and Earth Science, National Oceanography Centre Southampton, University of Southampton, UK

[7]School of Earth and Ocean Sciences, Cardiff University, UK

The interplay between ocean circulation and biological productivity affects atmospheric CO_2 levels and marine oxygen concentrations. During the warming of the last deglaciation, the North Pacific experienced a peak in productivity and widespread hypoxia, with changes in circulation, iron supply, and light limitation all proposed as potential drivers. Here we use the boron-isotope composition of planktic foraminifera from a sediment core in the western North Pacific to reconstruct pH and dissolved CO_2 concentrations from 24,000 to 8,000 years ago. We find that the productivity peak during the Bølling-Allerød warm interval, 14,700 to 12,900 years ago, was associated with a

decrease in near-surface pH and an increase in pCO_2, and must therefore have been driven by increased supply of nutrient and CO_2-rich waters. In a climate model ensemble (PMIP3), the presence of large ice sheets over North America results in high rates of wind-driven upwelling within the subpolar North Pacific. We suggest that this process, combined with collapse of North Pacific Intermediate Water formation at the onset of the Bølling-Allerød, led to high rates of upwelling of water rich in nutrients and CO_2, and supported the peak in productivity. The respiration of this organic matter, along with poor ventilation, likely caused the regional hypoxia. We suggest that CO_2 outgassing from the North Pacific helped to maintain high atmospheric CO_2 concentrations during the Bølling-Allerød and contributed to the deglacial CO_2 rise.

The balance between the supply of nutrients and carbon to surface waters via ocean circulation and their removal via biological productivity is a first order control on atmospheric CO_2. This is particularly important at high latitudes[1,2], where Ekman suction, driven by cyclonic wind stress, and winter mixing supply CO_2 from the deep ocean to the surface. Depending on the availability of light and micronutrients, such as iron, this CO_2 may be captured by photosynthesis and returned to the deep ocean (the "biological pump"), or may escape to the atmosphere. The balance between circulation and biological productivity is also crucial for determining the ocean's dissolved oxygen content. Ventilation of the ocean at high latitudes mixes oxygen-rich waters from the surface into the ocean's interior, where oxygen is consumed

by the respiration of sinking organic matter, coupling the biogeochemical cycles of oxygen and carbon.

Dramatic changes in these biogeochemical balances are thought to occur during Pleistocene deglaciations, with reorganisations of circulation and productivity at high latitudes leading to changes in oceanic oxygen content and rapid atmospheric CO_2 rise[1-4]. However, the degree to which these changes in CO_2 and oxygen are driven by circulation versus biological productivity remains unknown, limiting our understanding of the mechanisms driving glacial-interglacial variations in CO_2 and climate. Particularly enigmatic are the dramatic peaks in productivity observed throughout the North Pacific Ocean during every deglaciation of at least the last ~1 Ma[5-8]. During the Bølling-Allerød interval (14.7-12.9 ka) of the last deglaciation (the only deglaciation for which we currently have records of intermediate-ocean redox) the productivity maximum is associated with widespread intermediate-ocean hypoxia in the North Pacific[3,9-11]. Since the discovery of these events more than 25 years ago[5,10] multiple explanations have been put forward, yet there is no consensus on the cause of either the productivity or the hypoxia; indeed the degree to which the productivity and hypoxia are linked, and even the direction of causation, are still contested. Some studies have proposed the productivity maximum was caused by an increase in the supply of nutrient and carbon rich waters[7,12], while others have suggested alleviation of iron[11,13] and/or light limitation as the main driver[14]. Early work debated the dominance of reduced ventilation versus increased productivity as the primary cause of the hypoxia[9,10], while more recently it has been proposed that hypoxia was

initially induced by subsurface warming, and that iron release from hypoxic sediments drove the increase in productivity[11].

Given the large reservoir of dissolved inorganic carbon (DIC) in the North Pacific interior[15] (Figure 1), a change in its supply and removal to and from the surface could have significant impact on the global carbon cycle, and play a role in glacial termination. Understanding the nature of these events is also important as they have been suggested to provide insights in to future changes in hypoxia and productivity in a rapidly warming climate[3,11].

Boron isotopes and CO_2 supply

To determine the cause of the Bølling-Allerød productivity maximum, we measured the boron isotope composition ($\delta^{11}B$) of the planktic foraminifera *N. pachyderma* from deglacial sediments in core MD01-2416 (51.27°N, 167.73°E, 2317 m water depth) (Methods). The core site is located close to the center of the high nutrient and CO_2 pool in the modern subpolar North Pacific (Figure 1), making it ideally suited to track changes in the biogeochemistry of the region. $\delta^{11}B$ is a proxy for seawater pH, which tracks seawater CO_2 chemistry, and with an estimate of one other parameter of the carbonate system (here alkalinity), allows the quantification of the CO_2 concentration of past seawater[16] (Methods).

Our results show a general decrease in near-surface pH over deglaciation, with a glacial high of 8.31±0.04 (1σ) falling to a value of 8.14±0.04 in the early

Holocene, identical to pre-industrial pH at 50m water depth[15] (Figure 2). Punctuating the general decline in pH is a pronounced pH minimum of 8.07±0.05 in the early Bølling-Allerød, coeval with the maximum in productivity. At this time, pCO_2 in the near surface ocean reached a maximum of 373±46 µatm (1σ) (Figure 3). The decrease in pH and increase in CO_2 demonstrates that the supply of carbon and nutrients to the surface ocean was greater than their removal by export production (Supplementary Figure 1). As export production during the Bølling-Allerød was higher than today[6,19], it follows that the supply of carbon and macronutrients must also have been higher.

PMIP3 model ensemble and paleo-circulation tracers

To investigate the physical mechanisms underlying the increase in nutrient and CO_2 supply, we looked for large-scale changes in the PMIP3 model ensemble[31] under glacial boundary conditions, alongside paleo-tracers of ocean circulation. Although formation of North Pacific Intermediate Water (NPIW) is extremely limited today[32], overturning circulation within the basin was significantly enhanced during the last glacial maximum (LGM): benthic foraminiferal $\delta^{13}C$ records indicate glacial expansion of NPIW to depths of >1500 m[29,33,34] (Supplementary Figure 2), flushing nutrients and carbon from intermediate waters and deepening the interior ocean nutrient/carbon reservoir. North Pacific ventilation may have been even deeper and more vigorous during early deglaciation[28,30,35], with possible localised deepwater formation during Heinrich Stadial 1[30,35,36] (HS1) potentially driving the early-

deglacial decrease in pH observed in our record (Methods). However, at the onset of the Bølling-Allerød a rapid decrease in benthic $\delta^{13}C$ and increase in benthic radiocarbon ages indicate a collapse in NPIW formation[28,30], and a circulation more similar to the modern[36] (Figure 3 and Supplementary Figure 3).

If the Bølling-Allerød was characterised by similar overturning circulation to today, why was the supply of nutrients and carbon to the surface ocean so much higher? All eight models in the PMIP3 ensemble show substantial increase in wind stress curl within the subpolar gyre under glacial boundary conditions, with an ensemble mean increase of ~60% relative to pre-industrial (Figure 4). This is driven by the presence of an ice sheet over North America, which causes a strengthening of the westerlies and a southward shift in the polar easterlies, substantially increasing meridional wind shear and associated upwelling by Ekman suction within the subpolar gyre.

At the onset of the Bølling-Allerød large ice sheets remained over North America, with the Laurentide Ice Sheet having lost only ~15% of its mass[37]. Ekman suction within the subpolar gyre would therefore have been significantly higher than modern. During the LGM, nutrient flushing by enhanced NPIW formation would have prevented the increase in Ekman suction from increasing the nutrient/carbon supply. However, following the collapse in NPIW at the onset of the Bølling-Allerød, the interior ocean nutrient/carbon reservoir would have shoaled, becoming accessible to the surface ocean (Supplementary Figure 3). This combination of nutrient- and

151 carbon- rich subsurface waters and enhanced Ekman suction led to a
152 substantial increase in nutrient and carbon supply to the surface.
153
154 **Nutrient utilisation and hypoxia**
155
156 Higher iron availability from atmospheric dust flux and the alleviation of light-
157 limitation in warm seasonally-stratified waters would have also helped Bølling-
158 Allerød productivity to exceed present-day levels[14,27] (Methods). However, our
159 pH and CO_2 record demonstrates that carbon and nutrient supply
160 overwhelmed iron and light availability, leaving a significantly higher
161 proportion of the upwelled macronutrients and carbon unutilised, and reducing
162 the net efficiency of the biological pump at this location. In contrast to $\delta^{11}B$,
163 foraminiferal $\delta^{15}N$ shows little change at the onset of the Bølling-Allerød
164 productivity maximum[19,22,25] (Figure 2). While no change in $\delta^{15}N$ during an
165 increase in productivity is consistent with an increase in nutrient supply[19],
166 previous interpretations have suggested increased nutrient supply was
167 balanced by higher export production, such that there was no net change in
168 the efficiency of the biological pump[19]. However, $\delta^{15}N$ is also influenced by the
169 isotopic composition of source water nitrate, which is thought to have
170 increased at the Bølling-Allerød due to enhanced denitrification associated
171 with regional hypoxia[22,25,26,38] (Figure 2). Signals of reduced nutrient
172 utilisation at the Bølling-Allerød are thus likely to be somewhat masked or
173 delayed in $\delta^{15}N$ records (Methods).
174

The increase in export production during the Bølling-Allerød would have increased organic matter respiration, consuming oxygen in the ocean's interior. The supply of oxygen to intermediate waters would also have been reduced, due to the collapse in NPIW formation. Both processes thus contributed to the regional hypoxia observed at this time. The initiation of hypoxia may have acted as a positive feedback on productivity by increasing iron concentrations within upwelling waters[11], but it was not the primary cause of the increase in productivity.

Deglacial CO_2 rise

The increase in pCO_2 within the near-surface ocean at the onset of the Bølling-Allerød would have resulted in significant outgassing of CO_2, with our reconstructed ocean-atmosphere pCO_2 difference being ~130 µatm. Although *N. pachyderma* calcifies at around ~50 m water depth (Methods) the average annual pCO_2 difference between 50m depth and the surface ocean is only ~10 µatm at the core site today, thus the surface ocean would have also experienced elevated levels of CO_2 (Methods). A significant release of CO_2 is also supported by the warm temperatures recorded by the Mg/Ca of *N. pachyderma* during this time (Figure 3), which, as well as indicating a relatively near-surface habitat, would also have helped drive CO_2 outgassing from the ocean to atmosphere (Methods). Release of CO_2 from the subpolar Pacific at the onset of the Bølling-Allerød may have contributed to the rapid ~10 µatm increase in atmospheric CO_2 observed at this time[4,12] (Figure 3; Methods). Furthermore, continued CO_2 outgassing from the North Pacific

would have maintained the high levels of atmospheric pCO_2 observed throughout the Bølling-Allerød, countering the return to more stratified conditions in the Southern Ocean[4,16,39,40] and the ventilation of the Atlantic with low-preformed nutrient NADW[41], both of which should drive down atmospheric pCO_2. The upwelling of CO_2-rich waters in the North Pacific may thus allow atmospheric pCO_2 to stay high – rather than falling – during the Bølling-Allerød, and help drive continued deglaciation.

Results from ocean drilling in the Bering Sea indicate an expansion of NPIW during every glacial period of the last 1.2 million years[42]. All that is required for the model proposed here to explain the regular deglacial North Pacific productivity peaks is that the switch from the enhanced glacial mode of NPIW formation to the reduced interglacial mode precedes the loss of the Laurentide Ice Sheet and its associated enhanced Ekman suction. Brine rejection within the Bering Sea has been suggested as an important process by which NPIW formation was enhanced during glacial periods[42]. Over the last deglaciation there was an almost total loss of sea ice within the Bering Sea following the Northern Hemisphere warming at the Bølling-Allerød[43], however the Laurentide Ice Sheet did not ablate completely until ~7000 years later[37]. If the expansion of NPIW during glacial periods is driven by enhanced brine rejection, then the loss of sea ice prior to ice sheets during deglacial warming would dictate that increased upwelling of carbon and nutrient rich waters – and associated CO_2 release – would regularly occur during glacial terminations.

References

1. Toggweiler, J. R. Variation of Atmospheric CO_2 by Ventilation of the Ocean's Deepest Water. *Paleoceanography* **14,** 571–588 (1999).
2. Sigman, D. M., Hain, M. P. & Haug, G. H. The polar ocean and glacial cycles in atmospheric CO_2 concentration. *Nature* **466,** 47–55 (2010).
3. Jaccard, S. L. & Galbraith, E. D. Large climate-driven changes of oceanic oxygen concentrations during the last deglaciation. *Nature Geoscience* **5,** 151–156 (2011).
4. Marcott, S. A. *et al.* Centennial-scale changes in the global carbon cycle during the last deglaciation. *Nature* **514,** 616–619 (2014).
5. Keigwin, L., Jones, G. A. & Froelich, P. N. A 15,000 year paleoenvironmental record from Meiji Seamount, far northwestern Pacific. *Earth and Planetary Science Letters* **111,** 425–440 (1992).
6. Kohfeld, K. E. & Chase, Z. Controls on deglacial changes in biogenic fluxes in the North Pacific Ocean. *Quaternary Science Reviews* **30,** 3350–3363 (2011).
7. Jaccard, S. L. *et al.* Glacial/interglacial changes in subarctic North Pacific stratification. *Science* **308,** 1003–1006 (2005).
8. Jaccard, S. L., Galbraith, E. D., Sigman, D. M. & Haug, G. H. A pervasive link between Antarctic ice core and subarctic Pacific sediment records over the past 800kyrs. *Quaternary Science Reviews* **29,** 206–212 (2010).
9. Crusius, J., Pedersen, T. F., Kienast, S., Keigwin, L. & Labeyrie, L. Influence of northwest Pacific productivity on North Pacific Intermediate Water oxygen concentrations during the Bølling-Ållerød interval (14.7–

12.9 ka). *Geol* **32,** 633–636 (2004).

10. Behl, R. J. & Kennett, J. P. Brief interstadial events in the Santa Barbara basin, NE Pacific, during the past 60 kyr. *Nature* **379,** 243–245 (1996).

11. Praetorius, S. K. *et al.* North Pacific deglacial hypoxic events linked to abrupt ocean warming. *Nature* **527,** 362–366 (2015).

12. Galbraith, E. D. *et al.* Carbon dioxide release from the North Pacific abyss during the last deglaciation. *Nature* **449,** 890–893 (2007).

13. Mix, A. C. *et al.* in *Mechanisms of Global Climate Change at Millennial Time Scales* (eds. Clark, P. U., Webb, R. S. & Keigwin, L.) (American Geophysical Union, 1999). doi:10.1029/GM112p0127

14. Lam, P. J. *et al.* Transient stratification as the cause of the North Pacific productivity spike during deglaciation. *Nature Geoscience* **6,** 622–626 (2013).

15. Key, R. M., Olsen, A., van Heuven, S. & Lauvset, S. K. Global Ocean Data Analysis Project, Version 2 (GLODAPv2). *ORNL/CDIAC-162* (2015). doi:10.3334/CDIAC/OTG

16. Martínez-Botí, M. A. *et al.* Boron isotope evidence for oceanic carbon dioxide leakage during the last deglaciation. *Nature* **518,** 219–222 (2015).

17. Takahashi, T. *et al.* Climatological mean and decadal change in surface ocean pCO_2, and net sea–air CO_2 flux over the global oceans. *Deep Sea Research Part II: Topical Studies in Oceanography* **56,** 554–577 (2009).

18. Boyer, T. P. *et al. World Ocean Database 2013*. *NOAA Atlas NESDIS*

72, 209 (2013).

19. Ren, H. *et al.* Glacial-to-interglacial changes in nitrate supply and consumption in the subarctic North Pacific from microfossil-bound N isotopes at two trophic levels. *Paleoceanography* **30,** 1217–1232 (2015).

20. Key, R. M. *et al.* A global ocean carbon climatology: Results from Global Data Analysis Project (GLODAP). *Global Biogeochem. Cycles* **18,** GB4031 (2004).

21. Gebhardt, H. *et al.* Paleonutrient and productivity records from the subarctic North Pacific for Pleistocene glacial terminations I to V. *Paleoceanography* **23,** PA4212 (2008).

22. Brunelle, B. G. *et al.* Glacial/interglacial changes in nutrient supply and stratification in the western subarctic North Pacific since the penultimate glacial maximum. *Quaternary Science Reviews* **29,** 2579–2590 (2010).

23. Jaccard, S. L. *et al.* Subarctic Pacific evidence for a glacial deepening of the oceanic respired carbon pool. *Earth and Planetary Science Letters* **277,** 156–165 (2009).

24. Barron, J. A., Bukry, D., Dean, W. E., Addison, J. A. & Finney, B. Paleoceanography of the Gulf of Alaska during the past 15,000 years: Results from diatoms, silicoflagellates, and geochemistry. *Marine Micropaleontology* **72,** 176–195 (2009).

25. Galbraith, E. D. *et al.* Consistent relationship between global climate and surface nitrate utilization in the western subarctic Pacific throughout the last 500 ka. *Paleoceanography* **23,** PA2212 (2008).

299 26. Hendy, I. L., Pedersen, T. F., Kennett, J. P. & Tada, R. Intermittent
300 existence of a southern Californian upwelling cell during submillennial
301 climate change of the last 60 kyr. *Paleoceanography* **19,** PA3007
302 (2004).
303 27. Serno, S. *et al.* Comparing dust flux records from the Subarctic North
304 Pacific and Greenland: Implications for atmospheric transport to
305 Greenland and for the application of dust as a chronostraphic tool.
306 *Paleoceanography* **30,** 583–600 (2015).
307 28. Max, L. *et al.* Pulses of enhanced North Pacific Intermediate Water
308 ventilation from the Okhotsk Sea and Bering Sea during the last
309 deglaciation. *Clim. Past* **10,** 591–605 (2014).
310 29. Keigwin, L. Glacial Age Hydrography of the Far Northwest Pacific
311 Ocean. *Paleoceanography* **13,** 323–339 (1998).
312 30. Okazaki, Y. *et al.* Deepwater Formation in the North Pacific During the
313 Last Glacial Termination. *Science* **329,** 200–204 (2010).
314 31. Braconnot, P. *et al.* Evaluation of climate models using palaeoclimatic
315 data. *Nature Clim. Change* **2,** 417–424 (2012).
316 32. Talley, L. D. Distribution and formation of North Pacific intermediate
317 water. *J. Phys. Oceanogr.* **23,** 517–537 (1993).
318 33. Max, L. *et al.* Evidence for enhanced convection of North Pacific
319 Intermediate Water to the low-latitude Pacific under glacial conditions.
320 *Paleoceanography* **32,** 41–55 (2017).
321 34. Matsumoto, K., Oba, T. & Lynch-Stieglitz, J. Interior hydrography and
322 circulation of the glacial Pacific Ocean. *Quaternary Science Reviews*
323 **21,** 1693–1704 (2002).

35. Rae, J. W. B. *et al.* Deep water formation in the North Pacific and deglacial CO_2 rise. *Paleoceanography* **29,** 645–667 (2014).

36. Cook, M. S. & Keigwin, L. Radiocarbon profiles of the NW Pacific from the LGM and deglaciation: Evaluating ventilation metrics and the effect of uncertain surface reservoir ages. *Paleoceanography* **30,** 174–195 (2015).

37. Ullman, D. J., Carlson, A. E., Anslow, F. S., LeGrande, A. N. & Licciardi, J. M. Laurentide ice-sheet instability during the last deglaciation. *Nature Geoscience* **8,** 534–537 (2015).

38. Deutsch, C., Sigman, D. M., Thunell, R. C., Meckler, A. N. & Haug, G. H. Isotopic constraints on glacial/interglacial changes in the oceanic nitrogen budget. *Global Biogeochem. Cycles* **18,** GB4012 (2004).

39. Anderson, R. F. *et al.* Wind-Driven Upwelling in the Southern Ocean and the Deglacial Rise in Atmospheric CO_2. *Science* **323,** 1443–1448 (2009).

40. Burke, A. & Robinson, L. F. The Southern Ocean's Role in Carbon Exchange During the Last Deglaciation. *Science* **335,** 557–561 (2012).

41. McManus, J. F., Francois, R., Gherardi, J. M. & Keigwin, L. Collapse and rapid resumption of Atlantic meridional circulation linked to deglacial climate changes. *Nature* **428,** 834–837 (2004).

42. Knudson, K. P. & Ravelo, A. C. North Pacific Intermediate Water circulation enhanced by the closure of the Bering Strait. *Paleoceanography* **30,** PA002840 (2015).

43. Méheust, M., Stein, R., Fahl, K., Max, L. & Riethdorf, J.-R. High-resolution IP25-based reconstruction of sea-ice variability in the western

North Pacific and Bering Sea during the past 18,000 years. *Geo-Mar Lett* **36,** 101–111 (2015).

Corresponding Author: WRG; wrg4@st-andrews.ac.uk

Acknowledgments

We thank Michael Sarnthein for providing core material and stimulating discussions, the 'B-team' for their accommodation in the National Oceanography Centre Southampton's laboratories, Anabel Mortes Rodenas for assistance with ICP-MS analysis at Cardiff University, and Jonathan Holmes for support throughout the project. We acknowledge the World Climate Research Programme's Working Group on Coupled Modelling for the coordination of CMIP and thank the climate modeling groups for producing and making available their model output (https://esgf-node.llnl.gov/search/cmip5/). We thank three anonymous reviewers for their thoughtful comments and detailed suggestions that substantially improved this paper. This work was funded by NERC studentship NE/I528185/1 awarded to W.R.G., NERC studentship NE/1492942/1 to B.T., NERC grant NE/N011716/1 awarded to J.W.B.R and A.B., and NERC grant NE/I013377/1 awarded to A.E.S.

Author contributions

W.R.G. and J.W.B.R. designed the study and wrote the manuscript; W.R.G., J.W.B.R, G.L.F., C.H.L., and A.E.S. were involved in the generation of the trace element and $\delta^{11}B$ data; R.C.W. analysed climate model output; all

374 authors contributed to the interpretation and preparation of the final
375 manuscript.
376
377 **Financial competing interests**
378 The authors declare no competing financial interests.
379
380 *Figure captions*
381
382 **Figure 1. CO_2 and nutrients in the modern subpolar North Pacific (a)**
383 annual surface ocean-atmosphere CO_2 flux[17], with contours of surface ocean
384 phosphate (PO_4) in μmol/kg[18]. The location of core MD01-2416 (51.27°N,
385 167.73°E, 2317 m water depth) is indicated by a star **(b)** upper water column
386 profiles of dissolved inorganic carbon (DIC) and phosphate in the western
387 subpolar North Pacific[15].
388
389 **Figure 2. Deglacial changes in the biogeochemistry of the subpolar**
390 **North Pacific (a)** δ^{11}B of *N. pachyderma* from MD01-2416 **(b)** pH with LOESS
391 smooth and 1σ and 2σ error envelope (Methods). The star shows pre-
392 industrial pH at this site[20] (50m water depth) and blue lines show equilibrium
393 pH (Methods) **(c)** Opal MAR from MD01-2416[21] (filled circles, inset-axis),
394 RAMA-PC-44[9] (triangles), PC13[22] (squares), ODP882[23] (open circles) and
395 SO202-07-6[19] (inverse triangles) **(d)** Excess U (dark pink) and Mo (light pink)
396 from EW0408-85JC[11,24] **(e)** δ^{15}N of *N. pachyderma* from SO202-07-6[19]
397 (diamonds), diatoms from PC13[22] (squares), and bulk sediments from MD01-
398 2416[25] (dashed line), ODP887[25] (solid line) and ODP1017[26] (dotted line) **(f)**

^{4}He flux from SO202-7-6[27]. YD, B/A and HS1 are the Younger Dryas, Bølling Allerød, and Heinrich Stadial 1. See supplement for core locations.

Figure 3. Deglacial temperature, pCO_2 and NPIW formation (a) *N. pachyderma* Mg/Ca-temperature with LOESS smooth and 1σ and 2σ error envelope. The star shows modern mean annual temperature at the site[18] (50m water depth) **(b)** pCO_2 in the atmosphere[4] and near-surface subpolar North Pacific with LOESS smooth and 1σ and 2σ error envelope (Methods). The star shows pre-industrial pCO_2 at the site[20] (50m water depth) **(c)** $\delta^{13}C$ of *Cibicidoides* spp. from the intermediate Bering Sea (SO201-2-85KL) and Okhotsk Sea (SO178-13-6)[28] (Methods). The triangle shows the LGM value for the intermediate-depth (~1000 m) Okhotsk Sea[29] **(d)** Benthic-planktic ^{14}C age difference in the intermediate depth (<1500 m) northwest Pacific[30] with 1σ error bars and LOESS smooth; CH84-14 (circles), GH02-1030 (triangles), and MR01K03-PC4/PC5 (diamonds). The star shows pre-bomb benthic-planktic ^{14}C age[20].

Figure 4. Wind stress curl in the glacial North Pacific. (a) PMIP3 ensemble mean difference in wind stress curl in the North Pacific in LGM relative to the pre-industrial (PI) control (positive means greater wind stress curl in LGM), with changes in vector windstress indicated by the arrows (see grey arrow in top left corner for scale) **(b)** PI and LGM windstress curl between 40°N and 60°N (shown by the black box in a, corresponding to the position of the subpolar gyre under PI conditions) in each of the models. The ensemble means for the PI and LGM are shown by the stars.

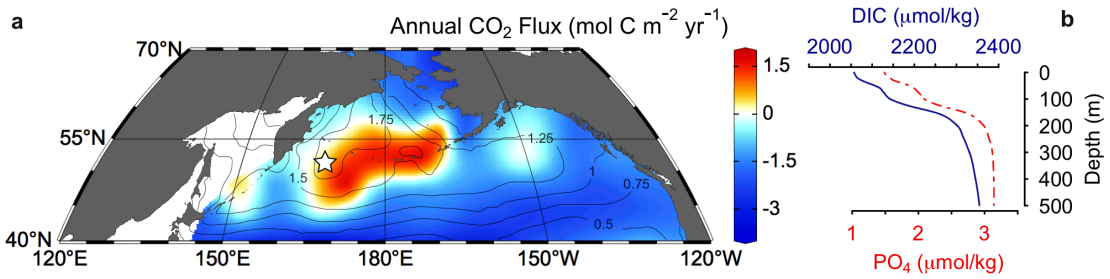
a
Annual CO2 Flux (mol C m-2 yr-1)
70°N
55°N
40°N
120°E
150°E
180°E
150°W
120°W
1.75
1.25
1.5
1
0.75
0.5
1.5
0
-1.5
-3
b
DIC (μmol/kg)
2000
2200
2400
0
100
200
300
400
500
Depth (m)
1
2
3
PO4 (μmol/kg)

Figure 1

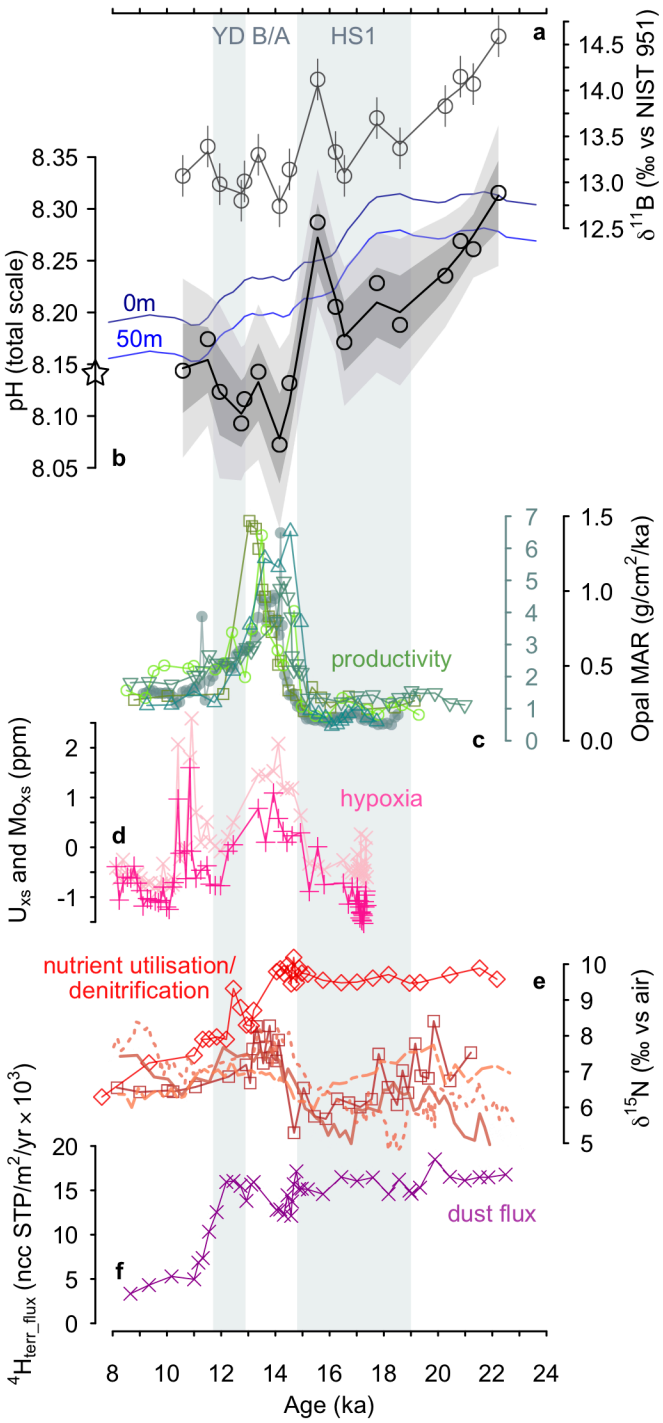
YD B/A
HS1
a
b
c
d
e
f
0m
50m
pH (total scale)
8.35
8.30
8.25
8.20
8.15
8.10
8.05
14.5
14.0
13.5
13.0
12.5
δ11B (‰ vs NIST 951)
productivity
7
6
5
4
3
2
1
0
1.5
1.0
0.5
0.0
Opal MAR (g/cm2/ka)
hypoxia
2
1
0
-1
Uxs and Moxs (ppm)
nutrient utilisation/
denitrification
10
9
8
7
6
5
δ15N (‰ vs air)
dust flux
20
15
10
5
0
4Hterr_flux (ncc STP/m2/yr x 10^3)
8
10
12
14
16
18
20
22
24
Age (ka)

Figure 2

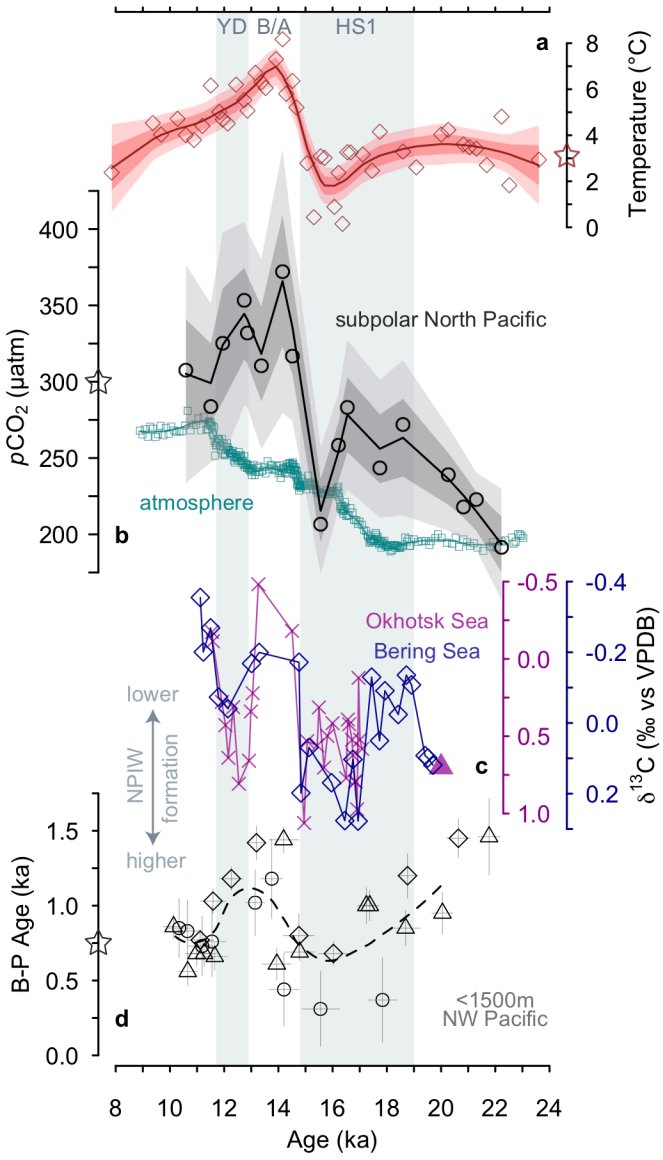
YD
B/A
HS1
a
Temperature (°C)
pCO2 (µatm)
subpolar North Pacific
atmosphere
b
Okhotsk Sea
Bering Sea
lower
NPIW
formation
higher
c
δ13C (‰ vs VPDB)
B-P Age (ka)
d
<1500m
NW Pacific
Age (ka)

Figure 3

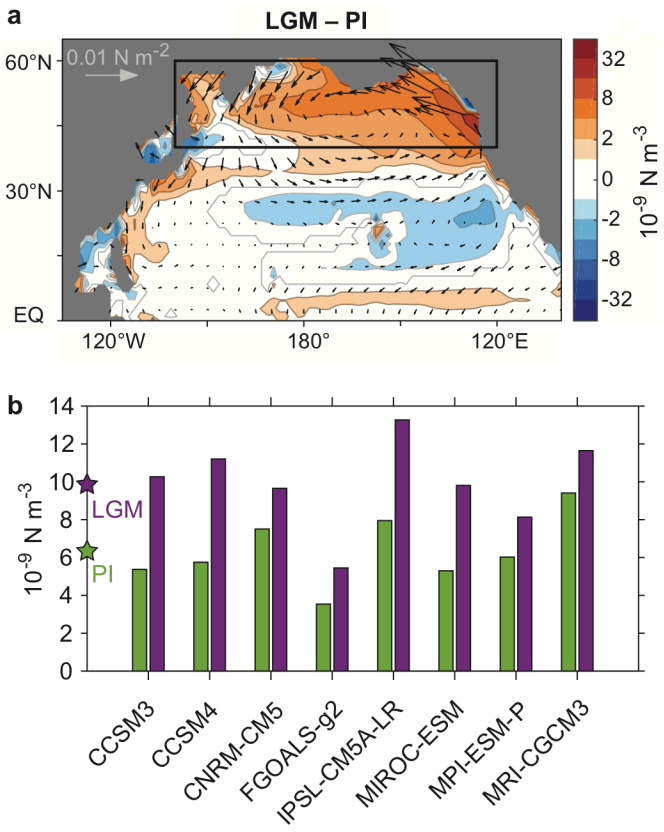
a
LGM – PI
0.01 N m-2
60°N
30°N
EQ
120°W
180°
120°E
32
8
2
0
-2
-8
-32
10-9 N m-3
b
14
12
10
8
6
4
2
0
10-9 N m-3
LGM
PI
CCSM3
CCSM4
CNRM-CM5
FGOALS-g2
IPSL-CM5A-LR
MIROC-ESM
MPI-ESM-P
MRI-CGCM3

Figure 4

Methods

Data availability

The authors declare that data supporting the findings of this study are available within the article and its supplementary information files. Data are also available on *Pangaea* (doi.pangaea.de/10.1594/PANGAEA.887381).

Habitat depth and seasonality of N. pachyderma in the western North Pacific

Sediment trap data in the modern NW Pacific display two seasonal *N. pachyderma* abundance peaks during the spring and autumn, roughly corresponding to the time of most, and least, stratification respectively. As these fluxes are more or less equal, the geochemical signature of *N. pachyderma* should represent mean annual oceanographic conditions at a water depth of ~50 m[44], provided that the growing season of *N. pachyderma* did not change substantially in the past.

Core materials

Core MD01-2416 was raised from 51.27°N, 167.73°E, 2317 m water depth on the Detroit Seamount. This site is situated within the subpolar North Pacific High Nutrient Low Chlorophyll zone, making it well suited to track past changes in CO_2 outgassing in this region (Figure 1). %Opal data from the core (Figure 2) were previously published (refs[21,45]), and were converted into mass accumulation rate (MAR) using the age model described below. Foraminifera are well-preserved throughout the deglaciation in this core, likely due to its high sedimentation rate and the relatively muted changes in carbonate ion since the LGM in the deep Pacific[46].

Age model for MD01-2416

We generated a new age model for the core by recalibrating 36 *N. pachyderma* ^{14}C dates from ref[47], excluding 6 ^{14}C dates previously demonstrated to show evidence of reworking[47]. The ^{14}C dates were calibrated with INTCAL13[48]. There are likely to be considerable changes in deglacial reservoir age which are difficult to constrain; we apply a constant reservoir age of 950±450 yrs, which encompasses the modern seasonal variability within the region, as well as paleo-reconstructions and model estimates for the LGM, deglaciation, and the Holocene[20,49-52]. The age model was constructed using the BACON[53] Bayesian age modelling package in R. Uncertainty in calibrated age is typically ±800 years at the 95% confidence interval, increasing to greater than ±1000 years before ~21ka. Using the ^{14}C plateau tuned chronology of ref[47] makes no difference to any of the conclusions drawn (Supplementary Figure 4).

δ^{11}B and trace element analysis

Well-preserved *N. pachyderma* were picked from the 150-250 µm size fraction at a 3-15 cm resolution. ~400 individuals were used per δ^{11}B analysis. Samples were cleaned in a class 100 clean lab at the National Oceanography Centre Southampton (NOCS) according to the 'Mg' method of ref[54] as detailed in ref[55]. A ~5% split of the cleaned foraminiferal samples was analysed after acidification for a suite of trace elements at NOCS using an Element II HR-ICP-MS against matrix matched standards. δ^{11}B was analysed at NOCS on a Neptune MC-ICP-MS following the method of ref[55,56], which involves removing

527 the sample matrix prior to analysis using anionic exchange resin, and sample-
528 standard bracketing to correct for instrument induced mass fractionation. Long
529 term reproducibility of this approach is ±0.23‰ at the 95% confidence
530 interval[57].
531
532 To increase the resolution of the Mg/Ca record, 26 additional samples were
533 analysed for trace elements only. Between 20-50 individual *N. pachyderma*
534 were cleaned following the oxidative/reductive protocol of ref[58]. The samples
535 were analysed at Cardiff University using an Element II HR-ICP-MS against
536 matrix-matched standards. The same standards were used at both Cardiff
537 University and NOCS to ensure consistency.
538
539 Average Al/Ca values are ~50 µmol/mol. Six samples have Al/Ca between
540 100-150 µmol/mol, however these samples do not display elevated Mg/Ca or
541 B/Ca indicating no influence of clay contamination. Average Mn/Ca for
542 samples cleaned using the 'Mg' method is 80 µmol/mol, whereas average
543 Mn/Ca for reductively cleaned samples is <10 µmol/mol. Despite the higher
544 Mn/Ca values of the 'Mg' cleaned samples, both datasets display very similar
545 Mg/Ca (after correction for preferential dissolution of high-Mg calcite during
546 reductive cleaning[54]) and B/Ca values downcore, indicating no influence of
547 Mn-Fe oxyhydroxide coatings. Previously published Mg/Ca data from MD01-
548 2416[21,45] show elevated values compared to the data cleaned by both the 'Mg'
549 method and the reductive method in this study, indicating a possible influence
550 of contamination, so are not used in our temperature reconstruction. Including
551 these data makes no difference to any of the conclusions drawn.

552

553 *Temperature record*

554 The Mg/Ca values were converted to temperature using the species specific
555 calibration of ref[59] (recalculated by ref[60]). Samples that had been reductively
556 cleaned were adjusted upward by 12.5% to account for preferential
557 dissolution of high-Mg calcite during reductive cleaning[54]. The data were fitted
558 with a non-parametric regression (LOESS) in R. The smoothing parameter (α)
559 was optimised using generalised cross validation (GCV). A Monte Carlo
560 approach was used to determine the most likely fit to the data, with the
561 LOESS smooth fitted to ten thousand realisations of the temperature data with
562 an uncertainty of ±2.3 °C (2σ), accounting for the 1.2 °C (2σ) calibration
563 error[59], and incorporating terms for uncertainty in salinity (±2 PSU [2σ] with a
564 sensitivity of 3%/PSU[61,62]), and pH (±0.2 pH units [2σ] with a sensitivity of -
565 7%/0.1 pH units[62,63]).

566

567 pH is known to affect planktic foraminiferal Mg/Ca with a sensitivity of ~-
568 7%/0.1 pH units[62,63]. While the pH minimum during the Bølling-Allerød may be
569 influencing the apparent Mg/Ca temperatures, this influence is likely to be
570 minimal. Firstly, as the absolute value of pH during the Bølling-Allerød
571 interval is broadly equivalent to pre-industrial (it is a large anomaly from
572 equilibrium due to lower atmospheric CO_2 concentrations during the Bølling-
573 Allerød) the effect of pH on absolute temperature will be negligible. Secondly,
574 the ΔpH at the onset of the Bølling-Allerød is ~0.15 units, so given a Mg/Ca
575 sensitivity of -7%/0.1 pH units, this could only account for a 10% increase in
576 Mg/Ca, or ~1-1.5 °C, considerably smaller than the ~5 °C warming indicated

by the Mg/Ca record at the onset of the Bølling-Allerød. The effect of higher pH during the LGM means our Mg/Ca temperature record is likely to be underestimating LGM temperature by ~1-1.5 °C. Dissolution can also effect foraminiferal Mg/Ca, though this influence is relatively minor in lower-Mg planktic foraminifera such as *N. pachyderma*[64]. LGM-Holocene changes in bottom water carbonate ion concentration are also relatively minor within the Pacific (~10 μmol/kg)[46], and our Mg/Ca data show no correlation with $\%CaCO_3$ in this core, so dissolution is unlikely to have a significant influence on our record. Our temperature record shows good agreement with the assemblage derived temperature record of ref[21,45] from the same core. Recent research found that the *G. ruber* Mg/Ca-temperature sensitivity is lower than the widely applied 9%/°C temperature sensitivity[62]; if future calibration work also demonstrates similar results for *N. pachyderma*, our Mg/Ca-temperature record may need minor revision.

Carbonate system calculations

To calculate pH the $\delta^{11}B$ of *N. pachyderma* was converted to seawater $\delta^{11}B_{borate}$ using the calibration of ref[65], where $\delta^{11}B_{borate} = \delta^{11}B_{Npachyderma} + 3.38\pm0.71‰$ (2σ). To fully explore the uncertainty associated with the calibration, we recalibrated the dataset of ref[65], varying the slope between 0.6 and 1.4 (which incorporates the range previously observed in all other species of planktic foraminifera, refs[16,66,67]) with a flat probability distribution, allowing the intercept to vary (see sensitivity test below). pH was calculated from $\delta^{11}B_{borate}$ using a seawater $\delta^{11}B$ value of 39.61‰[68] and the experimentally-determined fractionation factor of 1.0272[69] following ref[70]. The boric acid

602 dissociation constant (K_B) was calculated with the Mg/Ca temperature, and an
603 estimate of salinity generated by taking the salinity at the site today (33.0
604 PSU), and accounting for the whole ocean change in salinity over deglaciation
605 by scaling the 1.15 PSU glacial salinity increase of ref[71] to the sea level curve
606 of ref[72]. To fully propagate uncertainty in reconstructed pH a Monte-Carlo
607 approach was taken, with ten thousand realisations of the data accounting for
608 the uncertainties in the measurement of $\delta^{11}B_{Npachyderma}$, the conversion of the
609 $\delta^{11}B_{Npachyderma}$ to $\delta^{11}B_{borate}$, and of the uncertainty in the temperature and
610 salinity reconstructions on K_B using the confidence interval of the LOESS
611 temperature smooth and a salinity uncertainty of ±2 units (2σ). Typical
612 uncertainty on the pH reconstruction following this approach is ±0.084 (2σ),
613 which is chiefly due to the uncertainty in the offset between the $\delta^{11}B$ of *N.*
614 *pachyderma* and seawater $\delta^{11}B_{borate}$ (±0.078 2σ). Using a constant value of K_B
615 (i.e. constant temperature and salinity) has no major influence on
616 reconstructed pH values (see sensitivity test). Preservation has not been
617 shown to influence planktic $\delta^{11}B$[73].
618
619 An additional parameter of the carbonate system is required to calculate pCO_2
620 from pH, and total alkalinity is widely used[16,56,65]. Although modeling studies
621 can provide estimates of the change in alkalinity during the LGM[1,74], there are
622 few data-based constraints on its secular evolution over deglaciation. Here we
623 follow the approach of ref[16], taking a range in alkalinity between modern day
624 alkalinity at the site (2235 μmol/kg)[20] plus an estimate of the glacial alkalinity
625 increase based on the modeling results of refs[1,74] (+125 μmol/kg), and
626 modern day alkalinity at the site minus 25 μmol/kg, with a 'flat' probability

627 distribution between these values. With this approach there is an equal
628 probability of total alkalinity being at any value between 2210 and 2360
629 µmol/kg at any point in the record, fully exploring the likely range in alkalinity
630 without giving weight to any particular value. Note, this range in alkalinity is
631 cautious, being broadly equivalent to the range observed across the surface
632 of the entire open Pacific Ocean today[20]. The pCO_2 of seawater was
633 calculated using the *seacarb* package in R[75], using the constants of refs[76-78].
634 To fully propagate the uncertainty associated with each parameter ten
635 thousand realisations of pH, total alkalinity, temperature and salinity were
636 input, using the uncertainty on each parameter described above. Following
637 this approach, the total uncertainty associated with our pCO_2 estimates is
638 typically ±64 µatm (2σ), which again is chiefly due to the uncertainty in the
639 offset between $\delta^{11}B_{Npachyderma}$ and $\delta^{11}B_{borate}$ (±55 µatm). pCO_2 estimates are
640 almost entirely driven by the pH estimates (Supplementary Figure 5). Typical
641 pCO_2 uncertainty associated with the temperature uncertainty is ±2 µatm (2σ),
642 and the uncertainty associated with the salinity uncertainty is ±10 µatm (2σ).
643 Using either a constant 'modern minus 25 µmol/kg' or 'modern plus 125
644 µmol/kg' total alkalinity changes the pCO_2 values by only ±20 µatm.
645
646 Surface ocean pH at equilibrium with the atmosphere was calculated using
647 alkalinity calculated in the manner described above, and the atmospheric CO_2
648 record of ref[4]. Salinity (estimated in the manner described above) and Mg/Ca
649 temperature were used to constrain changes in dissociation constants.
650 Equilibrium pH at 50m is calculated by applying the modern surface-50m pH
651 gradient (-0.035 units); deviations from equilibrium pH therefore represent

changes in the carbonate system beyond those expected from changing atmospheric CO_2.

Both the pH and pCO_2 records were fitted with a LOESS smooth in R, with the smoothing parameter (α) determined by GCV. To determine the most likely fit to the data a LOESS smooth fitted to ten thousand realisations of the data, accounting for the uncertainties in the pH and pCO_2 estimates in the manner described above; this approach allows us to identify significant trends within the data and reduce uncertainty in our estimates.

Carbonate system sensitivity tests

As the current $\delta^{11}B_{calcite}$-$\delta^{11}B_{borate}$ calibration for *N. pachyderma* comes from a limited range in pH[65], application of this calibration to the NW Pacific requires extrapolation beyond the calibrated range. We tested the sensitivity of our results to the assumed slope of calibration, building on the test outlined in ref[79]. We re-calibrated the coretop data of ref[65], forcing the slope within the range previously observed in all other species of planktic foraminifera (refs[16,66,67]), while allowing the intercept to vary (Supplementary Figure 6). This exercise demonstrates that within the range previously observed in all other species of planktic foraminifera, the assumed slope of the $\delta^{11}B_{calcite}$-$\delta^{11}B_{borate}$ calibration makes no difference to any of the conclusions drawn in this study.

To provide a further constraint on the relationship between $\delta^{11}B_{Npachyderma}$ and $\delta^{11}B_{borate}$, we measured the $\delta^{11}B$ of *N. pachyderma* (following the method

described above) from Holocene sediments in core MD02-2489 (54.39°N, 148.92°E, 3640 m water depth), located in the eastern subpolar Pacific, where modern pH values are significantly higher than in the western subpolar Pacific. Comparing this data along with the Holocene $\delta^{11}B_{Npachyderma}$ data from site MD01-2416 to pre-industrial $\delta^{11}B_{borate}$ (calculated from ref[20]) shows excellent agreement with the *N. pachyderma* $\delta^{11}B_{calcite}$-$\delta^{11}B_{borate}$ calibration proposed by ref[65] over a range of $\delta^{11}B$ ~equivalent to our down-core reconstruction (Supplementary Figure 6).

To test the sensitivity of our pH and pCO_2 reconstructions to temperature, we calculated pH and pCO_2 assuming constant temperatures of 2 °C, 5 °C and 8 °C (broadly the deglacial range suggested by the Mg/Ca). Supplementary Figure 7 demonstrates that using a constant temperature in our carbonate system calculations would not have any effect on the main findings of this study. Compiling all available proxy temperature data in the western subpolar North Pacific demonstrates that using the reconstructed temperatures suggested by all available proxies (Mg/Ca, $U^{k'}_{37}$, TEX_{86}, foraminiferal assemblage transfer function; refs[21,80-82]) in our carbonate system calculations results in a substantial outgassing of CO_2 from the subpolar North Pacific during the Bølling-Allerød.

Overturning and CO_2 in early deglaciation

In addition to the large decrease in pH at the onset of the Bølling-Allerød, our record demonstrates a decrease in pH during early deglaciation, reaching a minimum in HS1. Benthic foraminiferal $\delta^{13}C$ and radiocarbon records show an

increase in overturning circulation during early deglaciation relative to the LGM[28,30], with possible local deepwater formation during HS1[30,35] (Supplementary Figure 8). The deepening of the overturning circulation during early-deglaciation would have allowed deeply sequestered nutrients and CO_2 to mix more vigorously through the water column[35], resulting in the observed decrease in pH and increase in CO_2 in the near-surface ocean, and outgassing of CO_2 to the atmosphere. The increase in overturning would have resulted in a deepening of the mixed layer, such that light may have become limiting to primary production[14]. A return to a shallower overturning circulation (similar to the LGM) during late-HS1 would have lessened the upward mixing of deep carbon, increasing pH. Note, removing the high-pH data point at ~15.5 ka makes no difference to any of the conclusions drawn in this study; even without this high-pH data point there is a ~0.1 pH unit decrease from the mean HS1 value going into the B/A, indicating a substantial increase in nutrient- and CO_2- supply.

Nutrient utilisation/denitrification controls on $\delta^{15}N$

Nitrogen isotope records may be influenced by both the degree of nitrate utilisation and the isotopic composition of nitrate in the source water[22,25,38,83,84]. The widespread hypoxia accompanying the Bølling-Allerød productivity maximum is thought to have significantly increased denitrification within the oxygen minimum zones of the northeast Pacific[22,26,83,84], driving up the $\delta^{15}N$ of seawater nitrate. This is reflected by the large increase in bulk sediment $\delta^{15}N$ in cores from the Mexican[83] and Californian[26] continental margins to the Alaskan gyre[25] (Figure 2). This signal is spread throughout the

subsurface North Pacific[25], influencing the $\delta^{15}N$ of nitrate upwelled in the northwest Pacific. Records of $\delta^{15}N$ from the northwest Pacific (including bulk-sediment, diatom-bound, and foram-bound $\delta^{15}N$) show relatively muted changes at the onset of the Bølling-Allerød[19,22,25]. This likely reflects the opposing influences of a decrease in nutrient utilisation, due to higher nutrient supply in this key upwelling region, and the increase in $\delta^{15}N$ of source water nitrate due to hypoxia-driven denitrification.

Constraints on CO_2 uptake within the mixed layer

CO_2 concentrations in the mixed layer are likely to be lower than at the ~50m depth habitat of *N. pachyderma*. However, the mean annual difference between 50 m and surface ocean at this core site today is only ~10 µatm. During the summer months this difference is 21.9 µatm[20], due export production from the mixed layer, and during winter is close to zero due to mixing of the upper water column. While it is possible this difference was higher in the past, the Mg/Ca of the *N. pachyderma* indicates temperatures of 5-7 °C during the interval of low pH/high CO_2 suggesting that either (a) the *N. pachyderma* are recording a signal close to the surface at this time, (b) the mixed layer was deeper and thus thermal stratification weak, or (c) the *N. pachyderma* are recording a summer signal at this time, which would make the CO_2 concentrations a minimum estimate. All of these scenarios would result in a significant flux of CO_2 to the atmosphere.

CO_2 outgassing and atmospheric CO_2 change

751 Net changes in atmospheric CO_2 on millennial timescales are strongly
752 influenced by the inventory of preformed versus remineralised nutrients in the
753 ocean's interior[74,85]. Constraining preformed nutrient inventory is challenging
754 using paleo-proxies. However, given the increased nutrient consumption[19]
755 and high pH/low CO_2 of the near-surface North Pacific during the LGM
756 (Figures 1 and 2), Glacial NPIW would likely have had lower preformed
757 nutrient content than the water in the upper 1500m of the North Pacific
758 today[86]. Overall this would make the biological pump more efficient at the
759 LGM, driving down atmospheric CO_2. At the onset of the Bølling-Allerød, our
760 data suggest a net weakening in the strength of the North Pacific biological
761 pump and substantial outgassing of CO_2 from near surface waters. The
762 collapse in NPIW formation at this time would also have removed this source
763 of relatively low-preformed nutrient water from the ocean's interior, and thus
764 would also act to increase atmospheric CO_2.
765
766 *Benthic $\delta^{13}C$ records*
767 The benthic $\delta^{13}C$ records (*Cibicidoides* spp.) were corrected for the whole
768 ocean change in $\delta^{13}C$ relating to changes in the terrestrial biosphere by
769 scaling the value of ref[87] to global sea level[72]. This only affects the long-term
770 trend, and makes no difference to millennial scale events within the records.
771
772 *PMIP3 model output*
773 We analyse the difference in North Pacific wind-stress curl between LGM and
774 Preindustrial (PI) conditions as represented by 8 coupled climate models
775 (listed in Figure 4b). All models but CCSM3 are part of the Coupled Model

776 Intercomparison Project phase 5 (CMIP5). Orbital parameters, atmospheric
777 greenhouse gas concentrations, coastlines, and ice topography for the LGM
778 simulations are standardized as part of the Paleoclimate Model
779 Intercomparison Project phase 3 (PMIP3) and represent best estimates of the
780 climate state at the LGM, 21 ka before present[10]. We include data from
781 comparable LGM and PI simulations[88,89] using an older model, CCSM3, used
782 extensively in paleoclimate studies. We compute the wind stress curl
783 climatology based on the atmospheric output of each model. The computed
784 wind stress curl is linearly interpolated onto a common grid to compute the
785 ensemble mean (Figure 4a). Individual model results are shown on
786 Supplementary Figure 9.
787
788 **References only in Methods**
789
790 44. Kuroyanagi, A., Kawahata, H. & Nishi, H. Seasonal variation in the
791 oxygen isotopic composition of different-sized planktonic foraminifer
792 *Neogloboquadrina pachyderma* (sinistral) in the northwestern North
793 Pacific and implications for reconstruction of the paleoenvironment.
794 *Paleoceanography* **26,** PA4215 (2011).
795 45. Sarnthein, M. *et al.* Mid Holocene origin of the sea-surface salinity low
796 in the subarctic North Pacific. *Quaternary Science Reviews* **23,** 2089–
797 2099 (2004).
798 46. Yu, J. *et al.* Responses of the deep ocean carbonate system to carbon
799 reorganization during the Last Glacial-interglacial cycle. *Quaternary*
800 *Science Reviews* **76,** 39–52 (2013).

801 47. Sarnthein, M., Schneider, B. & Grootes, P. M. Peak glacial ^{14}C
802 ventilation ages suggest major draw-down of carbon into the abyssal
803 ocean. *Clim. Past* **9,** 2595–2614 (2013).
804 48. Reimer, P. J. *et al.* IntCal13 and Marine13 radiocarbon age calibration
805 curves 0-50,000 years cal BP. *Radiocarbon* **55,** 1869–1887 (2013).
806 49. Takahashi, T., Olafsson, J., Goddard, J. G., Chipman, D. W. &
807 Sutherland, S. C. Seasonal variation of CO_2 and nutrients in the high-
808 latitude surface oceans: A comparative study. *Global Biogeochem.*
809 *Cycles* **7,** 843–878 (1993).
810 50. Butzin, M., Prange, M. & Lohmann, G. Readjustment of glacial
811 radiocarbon chronologies by self-consistent three-dimensional ocean
812 circulation modeling. *Earth and Planetary Science Letters* **317-318,**
813 177–184 (2012).
814 51. Kovanen, D. J. & Easterbrook, D. J. Paleodeviations of radiocarbon
815 marine reservoir values for the northeast Pacific. *Geol* **30,** 243–246
816 (2002).
817 52. Southon, J. R., Nelson, D. E. & Vogel, J. S. A record of past ocean-
818 Atmosphere radiocarbon differences from the northeast Pacific.
819 *Paleoceanography* **5,** 197–206 (1990).
820 53. Blaauw, M. & Christen, J. A. Flexible paleoclimate age-depth models
821 using an autoregressive gamma process. *Bayesian Analysis* (2011).
822 doi:10.1214/11-BA618
823 54. Barker, S., Greaves, M. & Elderfield, H. A study of cleaning procedures
824 used for foraminiferal Mg/Ca paleothermometry. *Geochem. Geophys.*

825 *Geosyst.* **4,** 8407 (2003).
826 55. Rae, J. W. B., Foster, G. L., Schmidt, D. N. & Elliott, T. Boron isotopes
827 and B/Ca in benthic foraminifera: Proxies for the deep ocean carbonate
828 system. *Earth and Planetary Science Letters* **302,** 403–413 (2011).
829 56. Foster, G. L. Seawater pH, pCO_2 and [CO_3^{2-}] variations in the
830 Caribbean Sea over the last 130 kyr: A boron isotope and B/Ca study of
831 planktic foraminifera. *Earth and Planetary Science Letters* **271,** 254–266
832 (2008).
833 57. Foster, G. L. *et al.* Interlaboratory comparison of boron isotope analyses
834 of boric acid, seawater and marine CaCO3 by MC-ICPMS and NTIMS.
835 *Chemical Geology* **358,** 1–14 (2013).
836 58. Boyle, E. A. & Keigwin, L. Comparison of Atlantic and Pacific
837 paleochemical records for the last 215,000 years: Changes in deep
838 ocean circulation and chemical inventories. *Earth and Planetary*
839 *Science Letters* **76,** 135–150 (1985).
840 59. Elderfield, H. & Ganssen, G. Past temperature and δ18O of surface
841 ocean waters inferred from foraminiferal Mg/Ca ratios. *Nature* **405,** 442–
842 445 (2000).
843 60. Jonkers, L., Jiménez-Amat, P., Mortyn, P. G. & Brummer, G.-J. A.
844 Seasonal Mg/Ca variability of N. pachyderma (s) and G. bulloides:
845 Implications for seawater temperature reconstruction. *Earth and*
846 *Planetary Science Letters* **376,** 137–144 (2013).
847 61. Hönisch, B. *et al.* The influence of salinity on Mg/Ca in planktic
848 foraminifers – Evidence from cultures, core-top sediments and
849 complementary $\delta^{18}O$. *Geochimica et Cosmochimica Acta* **121,** 196–213

(2013).

62. Gray, W. R. *et al.* The effects of temperature, salinity, and the carbonate system on Mg/Ca in *Globigerinoides ruber* (white): A global sediment trap calibration. *Earth and Planetary Science Letters* **482,** 607–620 (2018).

63. Evans, D., Wade, B. S., Henehan, M. J., Erez, J. & Müller, W. Revisiting carbonate chemistry controls on planktic foraminifera Mg/Ca: implications for sea surface temperature and hydrology shifts over the Paleocene–Eocene Thermal Maximum and Eocene–Oligocene transition. *Clim. Past* **12,** 819–835 (2016).

64. Regenberg, M., Regenberg, A., Garbe-Schönberg, D. & Lea, D. W. Global dissolution effects on planktonic foraminiferal Mg/Ca ratios controlled by the calcite-saturation state of bottom waters. *Paleoceanography* **29,** 127–142 (2014).

65. Yu, J., Thornalley, D. J. R., Rae, J. W. B. & McCave, N. I. Calibration and application of B/Ca, Cd/Ca, and $\delta^{11}B$ in Neogloboquadrina pachyderma (sinistral) to constrain CO_2 uptake in the subpolar North Atlantic during the last deglaciation. *Paleoceanography* **28,** 237–252 (2013).

66. Henehan, M. J. *et al.* A new boron isotope-pH calibration for Orbulina universa, with implications for understanding and accounting for 'vital effects'. *Earth and Planetary Science Letters* **454,** 282–292 (2016).

67. Henehan, M. J. *et al.* Calibration of the boron isotope proxy in the planktonic foraminifera Globigerinoides ruber for use in palaeo-CO_2 reconstruction. *Earth and Planetary Science Letters* **364,** 111–122

875 (2013).
876 68. Foster, G. L., Pogge von Strandmann, P. A. E. & Rae, J. W. B. Boron
877 and magnesium isotopic composition of seawater. *Geochem. Geophys.*
878 *Geosyst.* **11,** Q08015 (2010).
879 69. Klochko, K., Kaufman, A. J., Yao, W., Byrne, R. H. & Tossell, J. A.
880 Experimental measurement of boron isotope fractionation in seawater.
881 *Earth and Planetary Science Letters* **248,** 276–285 (2006).
882 70. Zeebe, R. E. & Wolf-Gladrow, D. A. *CO_2 in Seawater: Equilibrium,*
883 *Kinetics, Isotopes*. (Elsevier Oceanography Series, 2001).
884 71. Adkins, J. F., McIntyre, K. & Schrag, D. P. The salinity, temperature,
885 and $\delta^{18}O$ of the glacial deep ocean. *Science* **289,** 1769–1773 (2002).
886 72. Lambeck, K., Rouby, H., Purcell, A., Sun, Y. & Sambridge, M. Sea level
887 and global ice volumes from the Last Glacial Maximum to the Holocene.
888 *Proceedings of the National Academy of Sciences* **111,** 15296–15303
889 (2014).
890 73. Edgar, K. M., Anagnostou, E., Pearson, P. N. & Foster, G. L. Assessing
891 the impact of diagenesis on $\delta^{11}B$, $\delta^{13}C$, $\delta^{18}O$, Sr/Ca and B/Ca values in
892 fossil planktic foraminiferal calcite. *Geochimica et Cosmochimica Acta*
893 **166,** 189–209 (2015).
894 74. Hain, M. P., Sigman, D. M. & Haug, G. H. Carbon dioxide effects of
895 Antarctic stratification, North Atlantic Intermediate Water formation, and
896 subantarctic nutrient drawdown during the last ice age: Diagnosis and
897 synthesis in a geochemical box model. *Global Biogeochem. Cycles* **24,**
898 GB4023 (2010).
899 75. Gattuso, J. P. *et al. Seacarb: seawater carbonate chemistry with R*. (R

900 Package version 3.1.2, 2017).
901 76. Millero, F. J., Graham, T. B., Huang, F., Bustos-Serrano, H. & Pierrot,
902 D. Dissociation constants of carbonic acid in seawater as a function of
903 salinity and temperature. *Marine Chemistry* **100,** 80–94 (2006).
904 77. Dickson, A. G. Standard potential of the reaction: AgCl(s)+1/2H_2 (g) =
905 Ag (s)+ HCl(aq), and and the standard acidity constant of the ion HSO
906 4^- in synthetic sea water from 273.15 to 318.15 K. *The Journal of*
907 *Chemical Thermodynamics* **22,** 113–127 (1990).
908 78. Dickson, A. G. & Riley, J. P. The estimation of acid dissociation
909 constants in seawater media from potentionmetric titrations with strong
910 base. I. The ionic product of water - K_W. *Marine Chemistry* **7,** 89–99
911 (1979).
912 79. Ezat, M. M., Rasmussen, T. L., Honisch, B., Groeneveld, J. &
913 deMenocal, P. Episodic release of CO2 from the high-latitude North
914 Atlantic Ocean during the last 135kyr. *Nature Communications* **8,** 1–10
915 (2017).
916 80. Riethdorf, J.-R., Max, L., Nürnberg, D., Lembke-Jene, L. & Tiedemann,
917 R. Deglacial development of (sub) sea surface temperature and salinity
918 in the subarctic northwest Pacific: Implications for upper-ocean
919 stratification. *Paleoceanography* **28,** 91–104 (2013).
920 81. Seki, O. *et al.* Reconstruction of paleoproductivity in the Sea of Okhotsk
921 over the last 30 kyr. *Paleoceanography* **19,** PA1016 (2004).
922 82. Seki, O. *et al.* Large changes in seasonal sea ice distribution and
923 productivity in the Sea of Okhotsk during the deglaciations. *Geochem.*
924 *Geophys. Geosyst.* **10,** Q10007 (2009).

83. Ganeshram, R. S., Pedersen, T. F., Calvert, S. E., McNeill, G. W. & R, F. M. Glacial-interglacial variability in denitrification in the world's oceans: Causes and consequences. *Paleoceanography* **15,** 361–376 (2000).

84. Brunelle, B. G. *et al.* Evidence from diatom-bound nitrogen isotopes for subarctic Pacific stratification during the last ice age and a link to North Pacific denitrification changes. *Paleoceanography* **22,** PA1215 (2007).

85. Ito, T. & Follows, M. J. Preformed phosphate, soft tissue pump and atmospheric CO2. *Journal of Marine Research* **63,** 813–839 (2005).

86. Talley, L. D. Closure of the global overturning circulation through the Indian, Pacific, and Southern Oceans: Schematics and transports. *oceanog* **86,** 80–97 (2013).

87. Peterson, C. D., Lisiecki, L. E. & Stern, J. V. Deglacial whole-ocean $\delta^{13}C$ change estimated from 480 benthic foraminiferal records. *Paleoceanography* **29,** 549–563 (2014).

88. Otto-Bliesner, B. L. *et al.* Climate sensitivity of moderate-and low-resolution versions of CCSM3 to preindustrial forcings. *J. Climate* **19,** 2567–2583 (2006).

89. Otto-Bliesner, B. L. *et al.* Last Glacial Maximum and Holocene Climate in CCSM3. *J. Climate* **19,** 2526–2544 (2006).

Supplementary Information

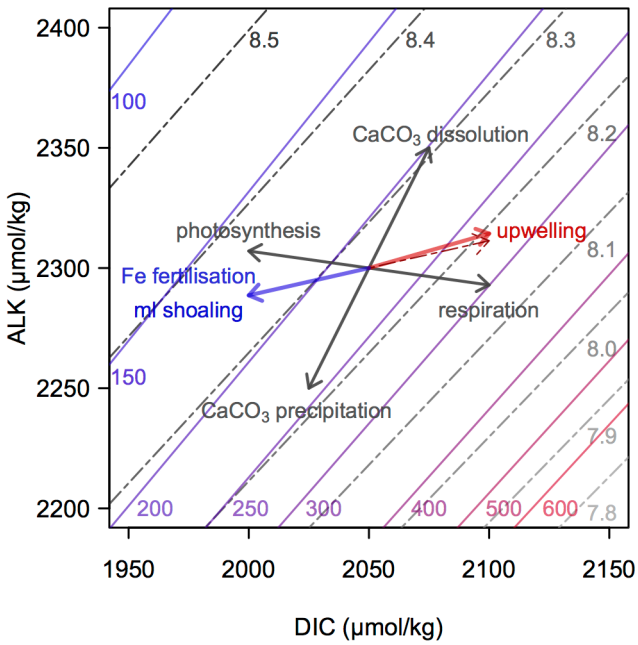

Supplementary Figure 1 Dissolved Inorganic Carbon (DIC) versus Alkalinity (ALK) with contours of pH on the total scale (grey dashed lines) and pCO_2 (coloured solid lines) at 5°C, 35 PSU and 0m water depth. The effects of photosynthesis and respiration, as well as the precipitation and dissolution of $CaCO_3$ are indicated by the grey arrows. Formation of organic matter by photosynthesis removes DIC and adds ALK in a ratio of ~7:1. Respiration of organic matter adds DIC and removes ALK in the same ratio. Precipitation of $CaCO_3$ removes both DIC and ALK with a ratio of 1:2 and dissolution of $CaCO_3$ adds DIC and ALK in the same ratio. The effects of an increase in export production from iron fertilisation and mixed layer shoaling are indicated by the blue arrow (assuming a C_{org}:$CaCO_3$ rain ratio of 4:1). The effect of an increase in upwelling of subsurface waters containing the respired/dissolved products exported from a surface ocean with a C_{org}:$CaCO_3$ rain ratio of 4:1 is shown by the solid red arrow; the effect of upwelling waters from 250m depth into the surface of the modern western subpolar North Pacific using the values from ref[15] is shown by the dashed red arrow. The upwelling of waters from the ocean's interior brings with it the respired products of photosynthesis, increasing the ratio of DIC to alkalinity (ALK), lowering pH and increasing CO_2 (red arrow). Increasing export production through the alleviation of iron or light limitation decreases the ratio of DIC/ALK, increasing pH and decreasing CO_2 (blue arrow).

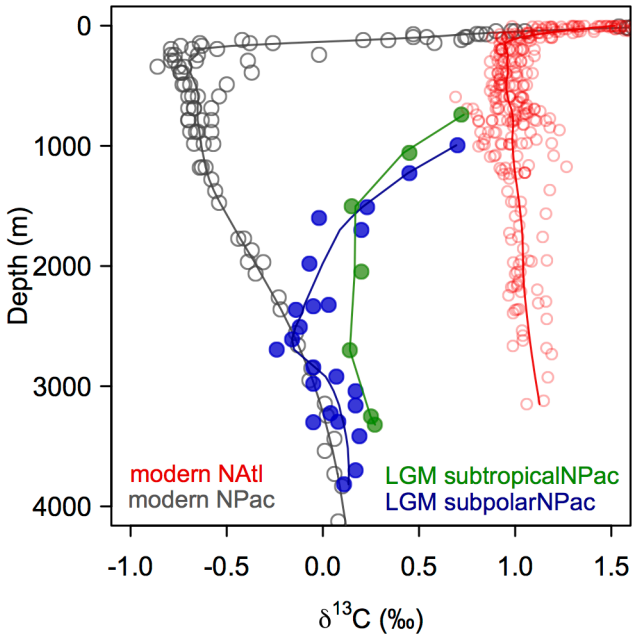

Supplementary Figure 2 $\delta^{13}C$ profiles of the modern (grey) and LGM (blue and green) NW Pacific, and modern North Atlantic (red). Modern values are DIC measurements from ref[15]. LGM values are *Cibicidoides* spp. from refs[29,34]. LGM values have been corrected for the whole ocean change in $\delta^{13}C$ using ref[87].

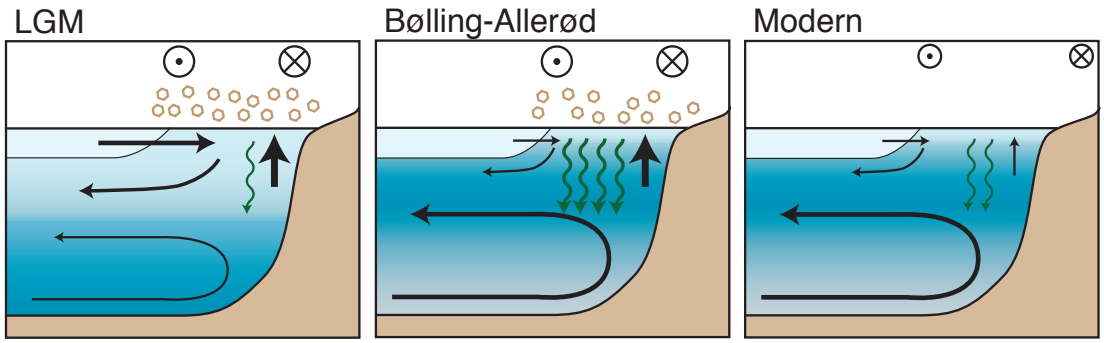

Supplementary Figure 3 Schematic of circulation and upwelling (black arrows), productivity (green arrows) and atmospheric iron supply (brown symbols) during the LGM, Bølling-Allerød, and in the modern North Pacific. At the LGM, ice sheets on North America shift the easterlies south and strengthen the westerlies, driving increased Ekman suction. However, the upwelled waters have relatively low nutrient contents, due to enhanced ventilation of the upper water column by NPIW, analogous to a shallower version of the modern North Atlantic. During the Bølling-Allerød warming NPIW collapses, increasing the nutrient content of subsurface waters. The continued presence of ice on North America maintains high Ekman upwelling, driving a high flux of nutrients and CO_2 into the surface. Relatively high iron availability from dust, along with reduced light limitation due to seasonal stratification, also contribute to high export productivity, but are not its primary cause. The linked combination of reduced ventilation and high productivity drives hypoxia at intermediate depths.

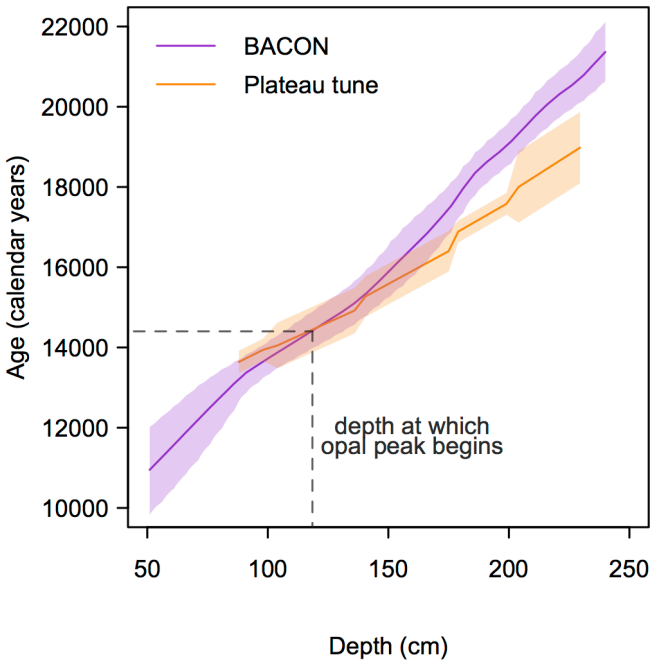

Supplementary Figure 4 New age model used in this study (purple), and previously published plateau-tuned age model of ref[47].

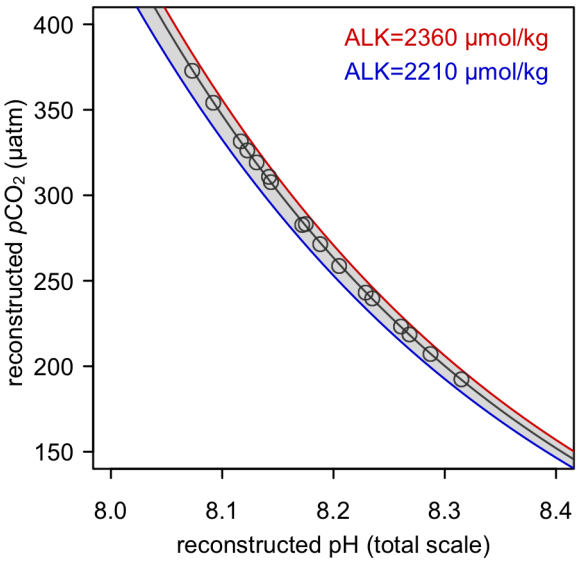

Supplementary Figure 5 Reconstructed pCO_2 as a function of reconstructed pH with varying alkalinity. The range in alkalinity represented by the shaded area is equivalent to the range in alkalinity found within the surface of the open Pacific Ocean today[15].

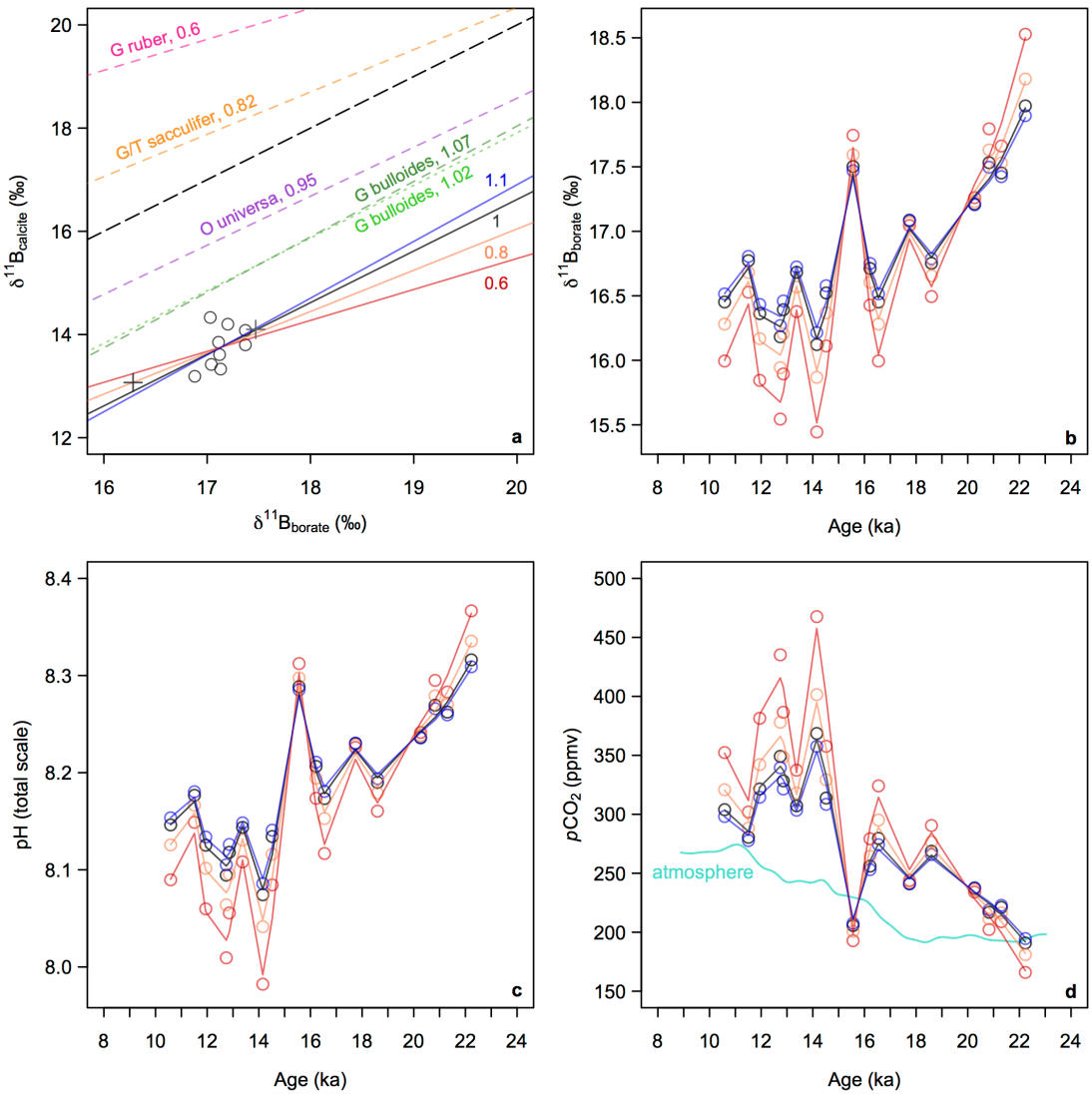

Supplementary Figure 6 $\delta^{11}B_{calcite}$-$\delta^{11}B_{borate}$ calibration sensitivity test **(a)** the dashed lines show all previously published planktic foraminiferal relationships between $\delta^{11}B_{borate}$ and $\delta^{11}B_{calcite}$ (refs[18,65,66]) with the slope of the relationship indicated. The 1:1 line is shown by the dashed black line. *N. pachyderma* coretop data of ref[65] are shown by the open circles. To test the sensitivity of our results to the assumed slope of the calibration line we re-calibrated the coretop data of ref[65], forcing the slope of the line within the range previously observed in all other species of planktic foraminifera (0.6 to 1.1, solid lines), and allowing the intercept to vary. Newly generated Holocene $\delta^{11}B_{Npachyderma}$ from MD01-2416 (dark-grey cross) and MD02-2489 (light-grey cross; 54.39°N, 148.92°E, 3640 m water depth) plotted against pre-industrial $\delta^{11}B_{borate}$, show very good agreement with the calibration proposed by ref[65] used in this study **(b)** down core $\delta^{11}B_{borate}$ **(c)** pH and **(d)** pCO_2 versus age (with LOESS smooth), assuming different slopes in relationship between $\delta^{11}B_{calcite}$ and $\delta^{11}B_{borate}$ (see panel a). This exercise demonstrates that within the range in slope previously observed in all other species of planktic foraminifera, the assumed slope of the $\delta^{11}B_{calcite}$-$\delta^{11}B_{borate}$ calibration makes no difference to any of the conclusions drawn in this study.

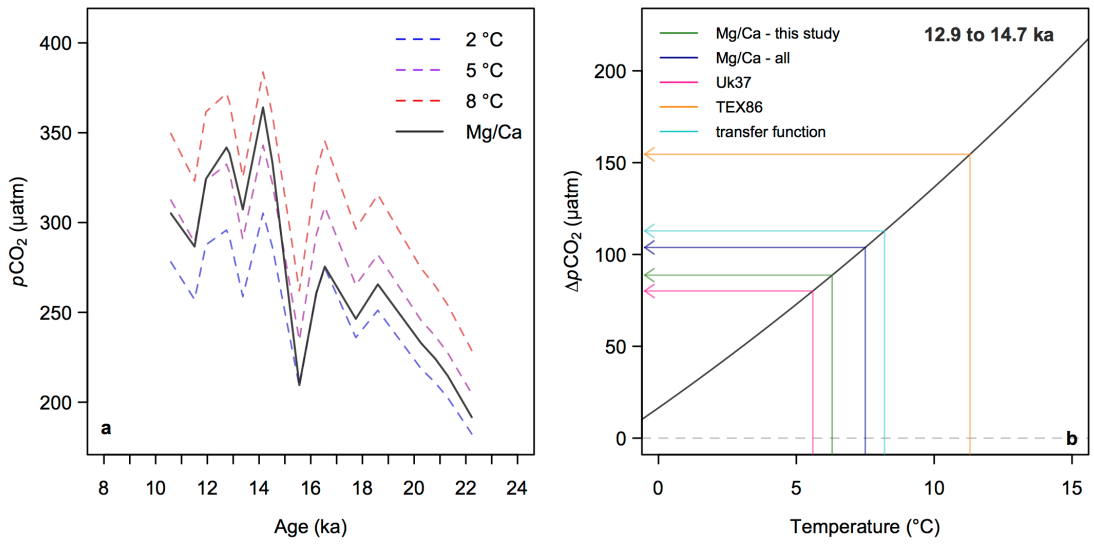

Supplementary Figure 7 Temperature-carbonate system sensitivity tests **(a)** reconstructed pCO_2 versus age at different temperatures (calculated at a constant salinity [33.9] and pressure [5 bar]). The coloured lines are calculated assuming a constant temperature of 2 °C, 5 °C and 8 °C, and the black line shows pH calculated using the Mg/Ca temperatures **(b)** average reconstructed ocean-atmosphere pCO_2 difference (ΔpCO_2) during the Bølling-Allerød (12.9 to 14.7 ka) as a function of temperature (using a salinity of 33.9 and pressure of 5 bar). Coloured lines show reconstructed temperature within the western subpolar North Pacific during this interval from all available proxy data (refs[21,80-82]). The temperatures suggested by all proxies suggest a substantial outgassing of CO_2 to the atmosphere during the Bølling-Allerød.

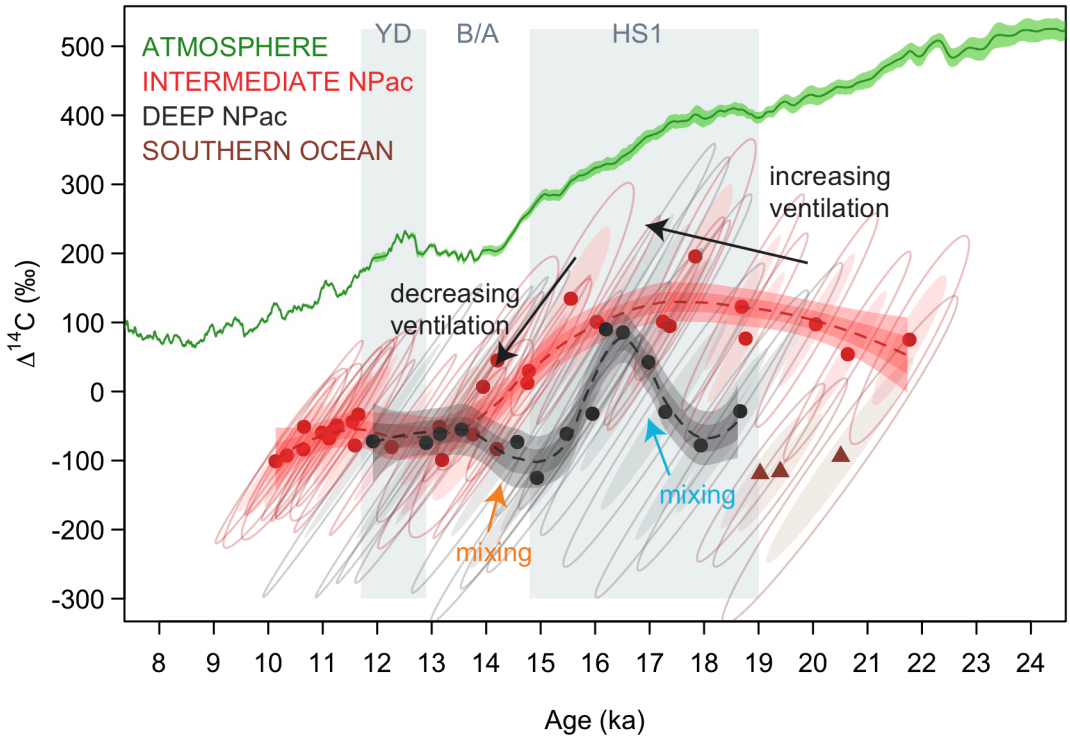

Supplementary Figure 8 Benthic $\Delta^{14}C$ records from the intermediate (<1500m) western North Pacific[30] (red circles, see caption of Figure 3 for core details) and deep North Pacific[35,47] (black circles), with the atmospheric record of ref[48] (green), and the LGM Southern Ocean data of ref[S1] (brown triangles). Confidence intervals are 95% (open circles) and 67% (filled circles). LOESS smooth shown by the dashed line with 67% and 95% confidence intervals. An increase in North Pacific overturning circulation is suggested during early deglaciation by increasing $\Delta^{14}C$, with deepwater formation in HS1 resulting in mixing throughout the water column to ~3600m (blue arrow). A reduction in intermediate water formation during the Bølling-Allerød results in old, radiocarbon depleted, deepwaters mixing throughout the water column, and low $\Delta^{14}C$ values at intermediate depths (orange arrow). The Southern Ocean record of ref[S1] is thought to represent southern sourced deepwater, which flows into the deep Pacific today, and likely during the LGM.

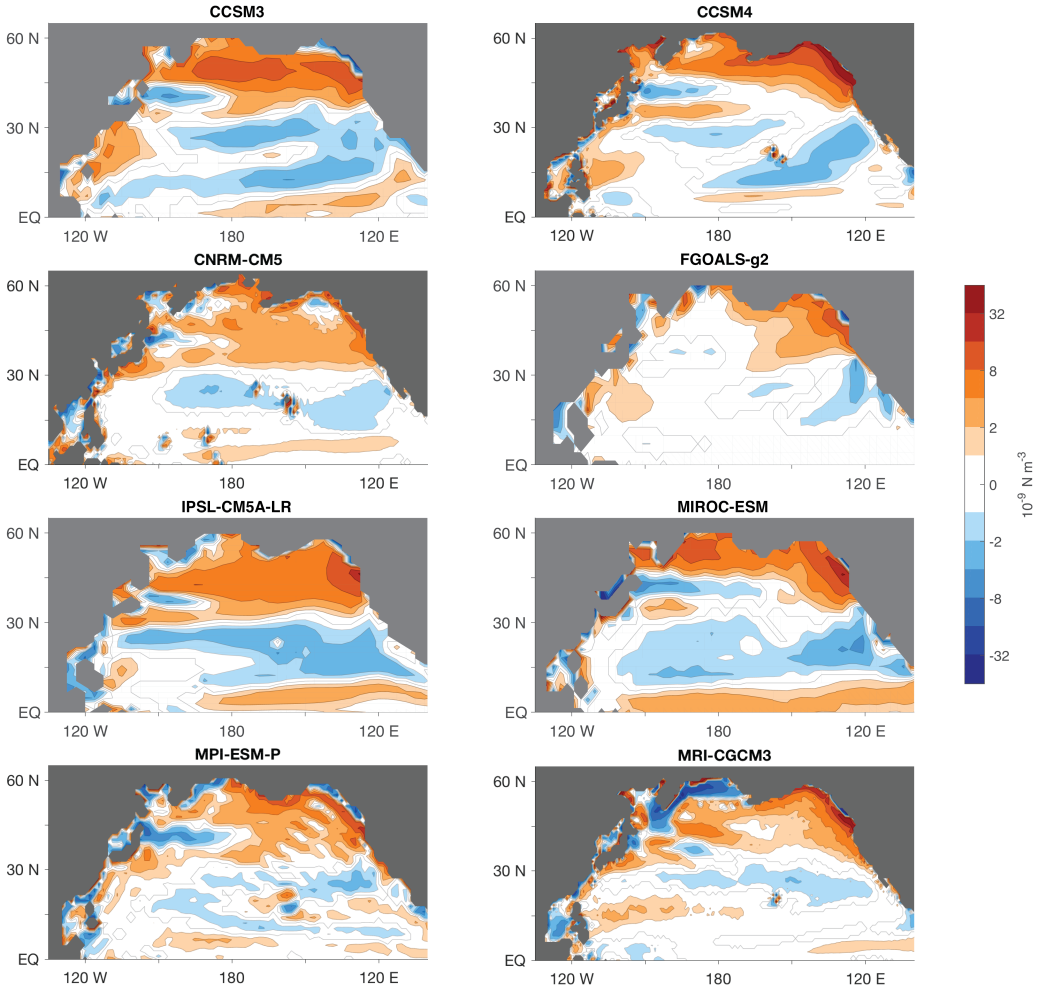

Supplementary Figure 9 Difference in wind stress curl within the North Pacific under glacial boundary conditions relative to pre-industrial control in PMIP3 climate model ensemble[31].

Supplementary Table 1

The location of cores in the North Pacific from which proxy data are discussed in the manuscript

Core	Lat (°N)	Lon (°E)	Water depth (m)
RAMA-PC-44	53.00	164.65	2980
PC13	49.72	168.31	2393
ODP882	50.37	167.60	3244
SO202-07-6	51.30	167.70	2345
EW0408-85JC	59.55	-144.15	682
ODP887	54.62	-148.75	3647
ODP1017	34.53	-121.10	955
SO201-2-85KL	57.51	170.70	968
SO178-13-6	52.73	144.71	713
CH84-14	41.73	142.55	978
GH02-1030	42.23	144.21	1212
MR01K03-PC4/PC5	41.12	142.40	1366

Supplementary References

S1. Skinner, L., Fallon, S., Waelbroeck, C., Michel, E. & Barker, S. Ventilation of the Deep Southern Ocean and Deglacial CO2 Rise. *Science* **328,** 1147–1151 (2010).